# Electrically Driven Microcavity Exciton-Polariton Optomechanics at 20 GHz

Alexander S. Kuznetsov,[1,†] Diego H. O. Machado,[1,2] Klaus Biermann,[1] and Paulo V. Santos[1,*]

[1]*Paul-Drude-Institut für Festkörperelektronik, Leibniz-Institut im Forschungsverbund Berlin e. V., Hausvogteiplatz 5-7, 10117 Berlin, Germany*

[2]*UNESP, São Paulo State University, Department of Physics, Av. Eng. Luiz Edmundo C. Coube 14-01, 17033-360, Bauru, São Paulo, Brazil*

(Received 20 June 2020; revised 17 February 2021; accepted 24 February 2021; published 23 April 2021)

Microcavity exciton polaritons enable the resonant coupling of excitons and photons to vibrations in the super-high-frequency (SHF, 3–30 GHz) domain. We introduce here a novel platform for coherent SHF optomechanics based on the coupling of polaritons and electrically driven SHF longitudinal acoustic phonons confined in a planar Bragg microcavity. The highly monochromatic phonons with tunable amplitudes are excited over a wide frequency range by piezoelectric transducers, which also act as efficient phonon detectors with a very large dynamical range. The microcavity platform exploits the long coherence time of polaritons as well as their efficient coupling to phonons. Furthermore, an intrinsic property of the platform is the backfeeding of phonons to the interaction region via reflections at the sample boundaries, which leads to quality factor × frequency products ($Q \times f$) exceeding $10^{14}$ Hz as well as huge modulation amplitudes of the optical transition energies exceeding 8 meV. We show that the modulation is dominated by the phonon-induced energy shifts of the excitonic polariton component. Thus, the large modulation leads to a dynamical switching of light-matter nature of the particles from a mixed (i.e., polaritonic) one to photonlike and excitonlike states at frequencies up to 20 GHz. On the one hand, this work opens the way for electrically driven polariton optomechanics in the nonadiabatic, sideband-resolved regime of coherent control. Here, the bidirectionality of the transducers can be exploited for light-to-sound-to-rf conversion. On the other hand, the large phonon frequencies and $Q \times f$ products enable phonon control with optical readout down to the single-particle regime at relatively high temperatures (of 1 K).

DOI: 10.1103/PhysRevX.11.021020

Subject Areas: Acoustics, Optoelectronics, Semiconductor Physics

## I. INTRODUCTION

The coherent coupling between photons and mechanical vibrations (termed optomechanics [1]) has experienced substantial theoretical and experimental advances since the initial investigations of parametric instabilities in Fabry-Perot interferometers [2] and of the coherent optical excitation of mechanical motion in the MHz range [3]. In particular, the demonstration of the strong optomechanical coupling in the MHz range [4], laser cooling of a microcavity (MC) to the mechanical ground state [5], quantum-coherent coupling of near-infrared photons and MHz phonons [6], and optomechanically induced transparency [7] constitute important landmarks in this field. Furthermore, the coupling of phonons to solid-state excitations is of relevance for quantum computations, communications, and metrology. Various quantum systems (e.g., spin and superconducting qubits) have internal resonances in the super-high-frequency (SHF, 3–30 GHz) range [8–10] of radio frequencies. Moreover, SHF phonons are attractive for coherent control in acousto-optics [11] as well as in systems for quantum-information processing. However, on-demand generation and detection of SHF phonons in low-loss materials as well as their efficient coupling to quantum systems constitute considerable challenges.

Most of the optomechanics studies have been carried out using vibrations with frequencies below 10 GHz. Planar solid-state structures like semiconductor superlattices and planar MCs are a promising platform for optomechanics at significantly higher frequencies. (Al,Ga)As MCs are particularly attractive for optomechanics since they can simultaneously confine in their active region both photons and longitudinal acoustic (LA) vibrations [12], thus enhancing the acousto-optical interaction by several orders of magnitude [13]. In fact, owing to a "double magic coincidence" of $Al_xGa_{1-x}As$ alloys [14], the ratio between their acoustic and optical impedances as well as between their LA and light propagation velocities are almost identical and

*Corresponding author.
santos@pdi-berlin.de
†Corresponding author.
kuznetsov@pdi-berlin.de

independent of the composition $x$. As a consequence, a MC optimized for photon confinement will also optimally confine acoustic phonons of the same wavelength with a comparable quality factor ($Q$) [14,15].

Vibrations with frequencies up to THz can be stimulated in these structures by short laser pulses, a technique known as picosecond (ps) acoustics [16]. The latter method has been applied as a complementary technique to Raman and Brillouin spectroscopy for basic studies of phonon propagation and confinement in layered structures [17–20]. The ability to generate strong and short strain pulses has been exploited for nonlinear acoustic effects [21] as well for the ultrafast control of emission centers inserted in layered structures [22–24].

Recent advances in the growth of high-quality MCs with embedded quantum wells have led to the emergence of MC exciton polaritons (simply, polaritons)—hybrid light-matter particles arising from the strong coupling between photons and quantum-well (QW) excitons. Polaritons inherit the low effective mass and long-range spatial coherence from their photonic component as well as strong nonlinearities associated with the excitonic component [25].

Microcavity polaritons have enabled the demonstration of multiple phenomena in the solid state, such as Bose-Einstein condensation [26], wavelike diffraction at defects and superfluidity [27], as well as parametric amplification, bistability [28], and topological effects [29] in the (10–300)-K temperature range. Although quantum polaritonics is still in its infancy, there has also been significant progress in the demonstration of quantum correlations at the single-particle level in polariton systems [30–32]. These recent developments have revealed a vastly unexplored potential of polaritons for quantum technologies [32,33].

Further motivation for polariton-based optomechanics, i.e., the coupling of polaritons to phonons, lies in the strength of the polariton interaction with vibrations. The latter value normally exceeds the one for bare photons since the photon-related radiation-pressure mechanism is complemented by the strong deformation potential modulation of the excitonic resonances [34,35]. In fact, light-scattering investigations of the polariton coupling to thermal LA phonons with frequencies of a few hundred GHz in superlattices [35,36] and MCs [37] yield photoelastic coupling enhancements at polariton resonance reaching $10^5$ [35].

Because of the strong coupling to phonons, optomechanics with MP polaritons not only offers an interface between the GHz and THz domains, but it also provides a means for the coherent coupling of optoelectronic excitations to mechanical motion down to the quantum limit. Polariton systems hold, therefore, considerable potential for testing fundamental limits as well as for advanced photonic applications.

Monochromatic strain fields induced by electrically excited surface acoustic waves (SAWs) have proven to be a powerful tool for the modulation and control of MC polaritons [38,39]. The finite penetration depth of the SAW fields, however, restricts the range of SAW frequencies for efficient coupling to polariton coupling to the sub-GHz domain. While several studies have addressed the modulation of excitonic systems in MCs by laser-excited phonons with frequencies of tens of GHz to THz, only very few have been carried out in the strong light-matter interaction (i.e., polariton) regime. Here, examples are the studies of nonadiabatic polariton modulation by laser-excited transient strain pulses [40–42]. The phonons, in these cases, are not monochromatic and, thus, not suitable for coherent control. There is clearly a technological gap for efficient generation of monochromatic strain in the tenth of GHz range. The demonstration of an electrically driven source of monochromatic GHz phonons and of the modulation of MC polaritons by such a source constitutes important milestones on the way toward coherent optomechanics in the GHz range.

In this work, we introduce a novel platform for electrically driven polariton optomechanics based on the piezoelectric generation and detection of bulk LA phonons (bulk acoustic waves, BAWs) in the SHF range using high-frequency piezoelectric BAW resonators (BAWRs) fabricated on the surface of a polariton MC [cf. Fig. 1(a)]. The studies are carried out in hybrid phonon-polariton MCs designed for the confinement of phonons with frequencies of 7 and 20 GHz. The highly monochromatic phonons are injected into MCs using BAWRs, which are driven by the external rf voltage. BAWRs generate highly monochromatic phonons (with tunable amplitudes) over a range of several GHz, which far exceeds the stop band of the phononic cavity. These resonators also act as highly sensitive phonon detectors, thus enabling acoustic echo spectroscopy with a very high (over 90 dB) dynamic range [43]. In this way, one can directly access the acoustic response of the MC and determine the distribution of the acoustic field within the samples. The latter distribution is found to be dictated by the resonant coupling of three acoustic cavities within the sample: The main one corresponding to the optical confinement region within the MC spacer, a surface cavity between the BAWR and the upper distributed Bragg reflector (DBR), and a bulk cavity formed between the lower DBR and the back surface of the wafer. We establish that the coupling enables the backfeeding of BAWs into the main cavity, thus resulting in acoustic quality factors $Q_a$'s significantly higher than the ones expected from the acoustic reflectivity of DBRs as well as in frequency $Q_a \times f_a$ products exceeding $10^{14}$.

The strong acoustic field in the MC spacer embedding the QWs induces a huge modulation of the polariton energies with amplitudes ($>8$ meV) exceeding the light-matter Rabi coupling. We also investigate the nature of the polariton-phonon coupling and show that the large energy modulation arises from the deformation potential coupling

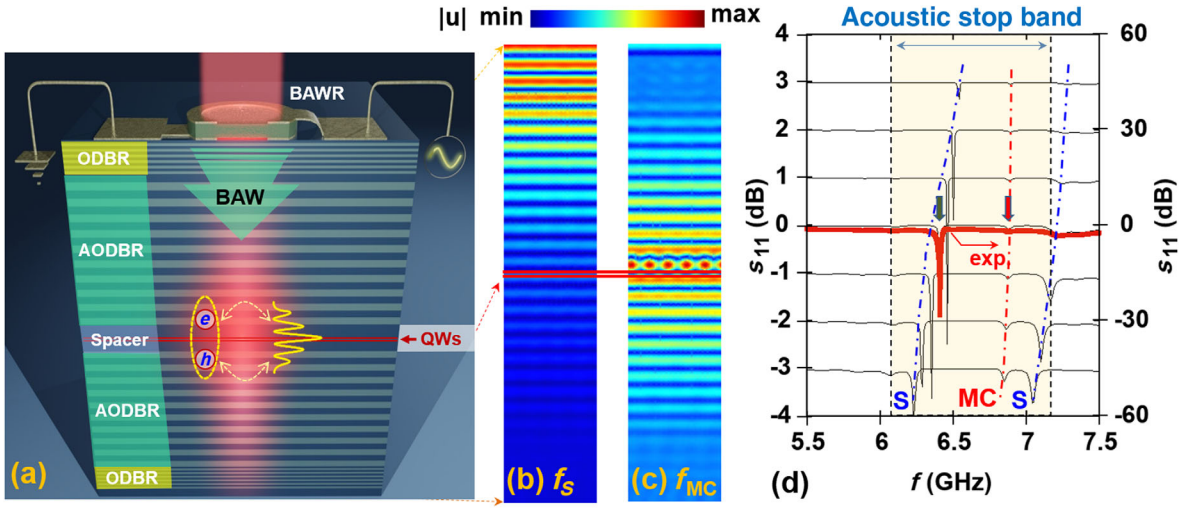


FIG. 1. Hybrid MC for polaritons and phonons. (a) Schematic cross section of sample $A$ showing the spatial distribution of photon (red-shaded region) and exciton-polariton fields (yellow). ODBR and AODBR stand for the distributed Bragg reflectors (DBRs) acting as optical and acoustic mirrors, respectively. Longitudinal bulk acoustic waves (BAWs) are generated by a ring-shaped bulk acoustic wave resonator (BAWR) driven by rf voltage. The ring-shaped BAWR has an aperture for laser excitation of the MC. (b),(c) Profiles for the acoustic displacement field $|\mathbf{u}|$ calculated for the mode localized (b) at the sample surface (mode with $f_S = 6.36$ GHz) and (c) within the MC spacer [$f_{MC} = 6.83$ GHz; cf. thick arrows in (d)]. (d) Measured $s_{11}$ rf-scattering parameter of the BAWR (thick red curve) and calculated $s_{11}$ profiles for different thicknesses $d_{ZnO}$ of the piezoelectric ZnO layer of the BAWR varying from 300 nm (bottom curve) to 180 nm (top curve) in steps of 20 nm (thin black lines). The calculations are done according to the procedure outlined in Ref. [43]. The colored area in (d) indicates the spectral extent of the acoustic stop band of the MC.

to the polariton excitonic components. The latter coupling far exceeds the radiation-pressure coupling to the photonic MC mode.

In the subsequent sections, we first describe the structure of the hybrid optomechanical MCs (Sec. II A) and of BAWRs employed for the generation and detection of SHF BAWs (Sec. II B). The propagation and quality factors of the acoustic modes of the MCs are considered in Secs. II C and II D, respectively. The results on the phonon-polariton interactions are presented in Sec. III. Specifically, the lateral enhancement of the resonant acoustic fields within the cavity is discussed in Sec. III A. Large acoustic modulation of the polariton energy is presented in Sec. III B followed by the elucidation of the modulation mechanism in Sec. III C. The implication of the large values of the quality factor × frequency products ($Q \times f$) is discussed in Sec. III D. Section IV summarizes the main results and prospects of this work.

## II. HYBRID OPTOMECHANICAL CAVITIES

### A. Microcavity structure

Polariton optomechanics profits from the ability of planar (Al,Ga)As MCs to simultaneously confine within their spacer region both photons and acoustic phonons with the same wavelength $\lambda_0$ [12,14,44]. This ability relies on the proportionality between the impedances and propagation velocities of light and mechanical waves in $Al_xGa_{1-x}As$ alloys with different compositions $x$ [14]. As a consequence, an (Al,Ga)As-based optical MC designed for the confinement of near-IR photons also confines longitudinal BAWs in the GHz range [14]. The ratios between the polariton and phonon energies are dictated by the corresponding ratio between their propagation velocities. The optomechanical coupling becomes strongly enhanced in these structures [37,38] not only due to the simultaneous confinement but also as a result of the increase of the photoelastic coupling at the polariton resonances [35].

The studies are carried out using hybrid acousto-optical (Al,Ga)As MCs with the structure displayed in Fig. 1(a) with spacer layers embedding (In,Ga)As QWs (see the Appendix A for details). We present experimental results obtained for two samples grown on GaAs (001) substrates by molecular beam epitaxy.

The first sample [designated as sample $A$ and illustrated schematically in Fig. 1(a)] has a special design to enable the simultaneous confinement of optical and acoustic modes of wavelengths $\lambda_o = 850/n_{GaAs}$ nm and $\lambda_a = 3\lambda_o$, respectively. Here, $n_{GaAs}$ is the GaAs refractive index. This sample thus confines photons with a (free-space) wavelength of 850 nm and phonons with a frequency of approximately 7 GHz within its spacer layer. Sample $A$ has two sets of distributed Bragg reflectors (DBRs). The inner set (i.e., the one enclosing the spacer) is an acousto-optical DBR [AODBR, cf. Fig. 1(a)] acting as a first-order and third-order grating for phonons and photons, respectively. It consists of ten $GaAs/Al_{0.85}Ga_{0.15}As$ layer pairs with $3\lambda_0/4$ thickness per layer. The outer set provides the additional optical confinement required to achieve the

strong coupling between photons and excitons for polariton formation designated as optical DBRs (ODBRs). Each of the ODBR stacks consists of six pairs of $\lambda_0/4$-thick $GaAs/Al_{0.85}Ga_{0.15}As$ layers. The spacer region of sample $A$ concurrently acts as an optical $5(\lambda_0/2)$ and as an acoustic $\frac{5}{3}(\lambda_0/2)$ MC spacer, as we discuss in detail in Appendix A. This region embeds two 15-nm-thick $In_{0.04}Ga_{0.96}As$ QWs separated by a 5-nm-thick GaAs barrier. The latter QWs are positioned at a depth corresponding to an antinode of the optical field and close to an antinode of the acoustic strain field inside the MC spacer.

According to the transfer-matrix simulations, sample $A$ has the optical quality factor $Q_{o,\mathrm{sim}} = 5600$ and the Rabi splitting $\Omega_{\mathrm{Rabi,sim}} = 4.3$ meV at 10 K (defined as twice the coupling energy between excitons and photon modes). The measured $\Omega_{\mathrm{Rabi}}$ is about 2 meV. Simulations for the acoustic field yield a bare (i.e., neglecting BAW reflections at sample borders) acoustic quality factor $Q_{a,\mathrm{sim}} = 172$ at 6.9 GHz at 10 K.

The second MC (sample $B$) has a $\lambda_0$-wide spacer embedding a single, 15-nm-thick $In_{0.04}Ga_{0.96}As$ QW. The AODBRs are designed as first-order reflectors for both photons and phonons with the same wavelength $\lambda_o = \lambda_a$, resulting in acoustic resonance frequencies close to 20 GHz [43]. The upper and lower AODBRs consist of 20 and 36 pairs of $\lambda_0/4$-thick $GaAs/Al_{0.85}Ga_{0.15}As$, respectively. The sample is in the strong-coupling regime at 10 K with a Rabi splitting energy $\Omega_{\mathrm{Rabi}} = 3$ meV.

While the hybrid MCs enable the simultaneous confinement of polaritons and phonons, it is not possible to perfectly overlap the antinodes of the acoustic and optical fields within the spacer layers. To enhance the coupling, special care is taken to position the QWs in between the antinodes of both the optical and acoustic fields (for details, see Appendix A). The QW position shift reduces the strain amplitude at the QWs by a factor $\eta_s \sim 0.8$ relative to the values at the strain antinodes.

### B. Bulk acoustic wave resonators

The BAWs are excited by BAWRs [43,45] fabricated on the sample surface, as illustrated schematically in Fig. 1(a). BAWRs consist of a piezoelectric ZnO film sandwiched between two 50-nm-thick metal contacts. The sputtered ZnO films have their hexagonal $c$ axis oriented perpendicular to the MC surface. Their thicknesses are chosen close to $d_{\mathrm{ZnO}} = \lambda_{\mathrm{BAW}}/2$, where $\lambda_{\mathrm{BAW}}$ is the acoustic wavelength (see Ref. [43] for details}. Under this condition, the acoustic response of a BAWR shows a single resonance at the frequency $f_{\mathrm{BAW}} = v_{\mathrm{BAW}}/\lambda_{\mathrm{BAW}}$, where $v_{\mathrm{BAW}}$ is the acoustic velocity [43]. A special feature of the BAWR design is the ring-shaped geometry with apertures in the bottom and top contacts for optical access to the MC. The piezoelectrically active area is thus defined by the overlap region of the top and bottom electrodes.

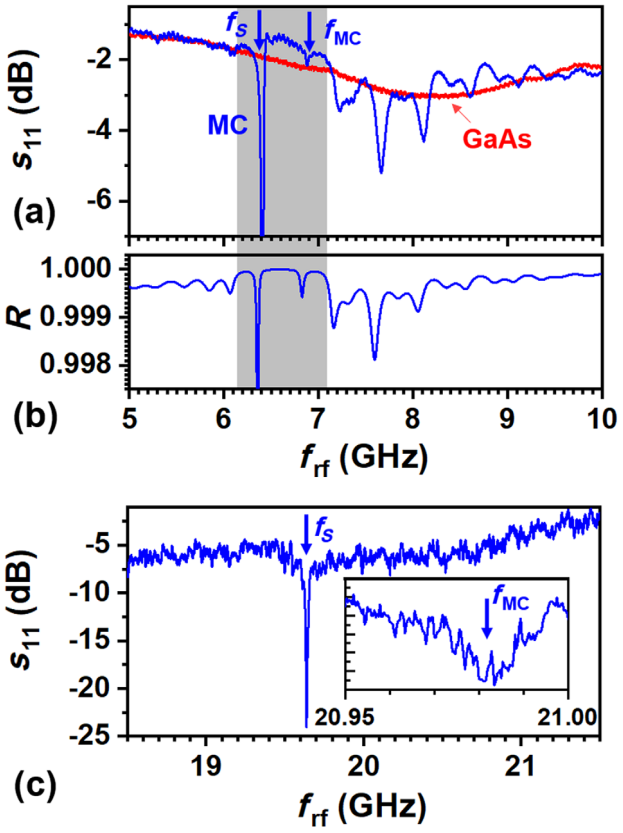


FIG. 2. (a) Electrical response of a BAWR on sample $A$ at 300 K. The red curve shows the $s_{11}$ scattering parameter for a BAWR on a bare GaAs substrate, while the blue one gives the response of a device on a MC (sample $A$). Both devices have nominally identical ZnO thickness of 260 nm. The gray-shaded area designates the spectral range of acoustic stop band created by the AODBR displayed in Fig. 1(a). The two modes within the stop band correspond to the MC acoustic mode with $f_{\mathrm{MC}} = 6.9$ GHz and the surface mode $f_S = 6.4$ GHz confined between the BAWR surface and the upper AODBR. (b) Simulated acoustic reflectivity of the MC with a BAWR device on its surface. (c) Electrical response of a BAWR on sample $B$ measured at 10 K, as given by the $s_{11}$ scattering parameter recorded as a function of the frequency. The curves are acquired using a BAWR with circular (rather than ring-shaped) contacts with a diameter of 20 $\mu$m.

The acoustoelectrical response of the samples is probed using a vector network analyzer to record its rf-power reflection coefficient (corresponding to the $s_{11}$ scattering parameter). The acoustic transduction results in the frequency-dependent attenuation of the reflected rf power, corresponding to the dips in the measured $s_{11}$.

Figure 2(a) compares the frequency response of BAWRs with a ZnO thickness of 280 nm deposited on a bare (001) GaAs substrate (red line) and on sample $A$. The minima in the $s_{11}$ spectra are signatures of BAW excitation: They arise from the reduction of the electrical reflection due to the excitation of acoustic modes within a broad resonance centered at 8 GHz. In contrast, the BAWR on sample $A$

develops a frequency spectrum characterized by multiple resonances [cf. Fig. 2(a)]. In particular, one identifies two main acoustic resonances—$f_S$ and $f_{MC}$—both located within the acoustic stop band, which is marked by the shaded background (the stop band in sample $A$ is at the lower flank for the BAWR emission band). Figure 2(b) shows the calculated acoustic reflection of sample $A$ using a transfer-matrix approach, which accurately reproduces all spectral features of the measured acoustic response.

In order to understand the nature of the modes within the stop band, we show in Fig. 1(d) finite-element calculations [43,46] of the $s_{11}$ response (thin lines) for varying thicknesses $d_{ZnO}$ of the ZnO layer. The latter calculations accurately reproduce the measured response of Fig. 2(a) for a ZnO thickness $d_{ZnO} = 240$ nm (thick line) slightly smaller than the nominal one. While the MC mode is essentially insensitive to $d_{ZnO}$, the $S$ mode shifts toward higher frequencies with decreasing $d_{ZnO}$. This behavior arises from the fact that the $S$ mode is confined between the upper AODBR and the BAWR surface, while the MC mode is concentrated in between AODBRs, as illustrated by the calculated mode profiles of Figs. 1(b) and 1(c), respectively.

The generation of 20-GHz BAWs in sample $B$ is carried out using BAWRs with nominally 80-nm-thick ZnO films. Figure 2(c) displays the electrical response of a BAWR consisting of circular electrodes with a diameter of 20 $\mu$m deposited on this sample. The $s_{11}$ spectrum shows a sharp dip associated with the surface mode $f_S = 19.63$ GHz. Because of the thick upper AODBR in this sample, the MC mode at $f_{MC}$ (cf. inset) interacts weakly with the BAWR, thus leading to a much weaker signature in the rf-reflection spectrum than the one for sample $A$.

### C. Phonons in hybrid microcavities

Detailed information about the spatial distribution of the acoustic modes within the MC can be obtained via an inverse Fourier transformation of the $s_{11}$ response over the frequency range of the acoustic stop band, which yields the impulse time response (or echo profiles) of the BAWRs. Figure 3(a)

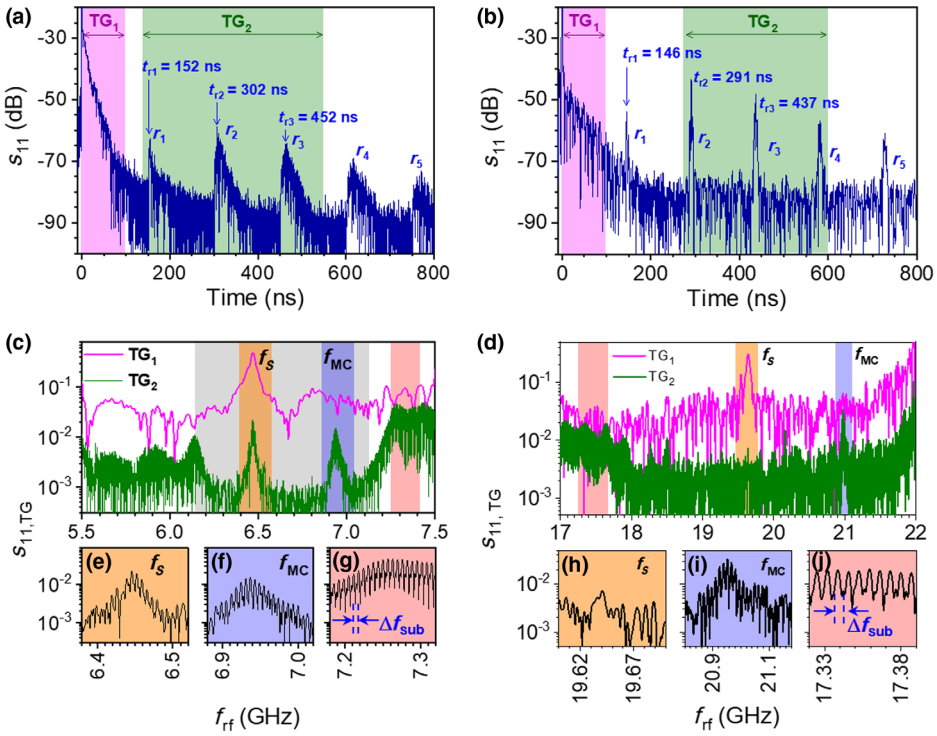


FIG. 3. Acoustoelectric response of sample $A$ [panels (a), (c), (e)–(g)] and sample $B$ [panels (b), (d), (h)–(j)] at 10 K. (a) Time dependence of the rf BAWR reflection of sample $A$ determined from the spectral response of the $s_{11}$ rf-scattering parameter in the (5.5–7.5)-GHz spectral range. The multiple acoustic echoes $r_i$ ($i = 1$ to 5) result from acoustic reflections at the back surface of the substrate. (c) Spectral dependence of the echoes within the time ranges $TG_1$ (0–100 ns, pink) and $TG_2$ (150–550 ns, green, encompassing three acoustic echoes) defined in (a). The gray area is the stop-band range. Two acoustic modes can be seen within the stop band for the $TG_2$ (see text for discussion). (e)–(g) Enlargements of the green curve in (c) highlighting the frequency comb with spacing $\Delta f_{sub} = 6.4$ MHz. (b) Time dependence of BAWR rf reflection of sample $B$ determined from the spectral response of the $s_{11}$ rf-scattering parameter in the (17–22)-GHz spectral range of Fig. 2(c). Similar to sample $A$, the multiple acoustic echoes $r_i$ ($i = 1$ to 5) are observed due to the acoustic reflections at the back surface of the substrate. (d) Spectral dependence of the echoes within the time ranges $TG_1$ (0–100 ns, pink) and $TG_2$ (270–600 ns, green, encompassing three acoustic echoes) defined in (b). Again, two acoustic modes can be seen within the stop band for the $TG_2$. (h)–(j) Enlargements of the green curve in (d) highlighting the frequency comb with spacing $\Delta f_{sub} = 6.9$ MHz.

shows the echo response of sample $A$, which is characterized by an exponentially decaying signal at short times ($<100$ ns denoted as the $TG_1$ range) followed by a series of echoes delayed by $t_{RT} = 151 \pm 1$ ns (region $TG_2$). The echoes are associated with round-trips of BAWs reflected at the backside of the double-polished GaAs substrate. Indeed, by taking the LA phonon velocity in GaAs $v_{LA} = 4.7$ $\mu$m/ns and the nominal substrate thickness $d_{sub} = 350 \pm 20$ $\mu$m, one obtains a round-trip time $2d_{sub}/v_{LA} = 149 \pm 15$ ns, which matches the echo delays $t_{RT}$ well. Only five reflections are shown in Fig. 3(a): In fact, up to nine echoes are detected, thus indicating long BAW propagation lengths. From the amplitude of the echoes, we determine BAW lifetimes exceeding 0.3 $\mu$s.

The contributions to the frequency response from different spatial regions can be identified by an inverse Fourier transformation of the time trace in Fig. 3(a) within the $TG_1$ and $TG_2$ time-delay regions. The results are shown in Fig. 3(c). The acoustic response at short times ($TG_1$ range) is dominated by a single strong resonance at $f_S = 6.46$ GHz corresponding to the surface cavity resonance mode of Fig. 1(b). The confinement near the surface by the upper AODBR accounts for the long decay time of the individual echo pulses in Fig. 3(a), which far exceeds the short transit time ($\sim 1/f_S = 0.15$ ns) across the BAWR. The spectrum obtained from the $TG_2$ time range shows two peaks (denoted as $f_S$ and $f_{MC}$) located on a wide background of low $s_{11,TG}$ response (gray-shaded area). The background is assigned to the acoustic stop band of the AODBRs, which can be detected due to the high dynamic range and time resolution (or, equivalently, wide frequency response) of the BAWRs. The two peaks at $f_S = 6.46$ GHz and $f_{MC} = 6.94$ GHz are attributed to acoustic modes of the surface ($S$) and the main (MC) cavities, respectively. The absence of the mode at $f_{MC}$ in the spectrum for the $TG_1$ is likely due to the large background induced by incomplete suppression of the electromagnetic contribution at short echo delays.

A closer examination of the frequency response for the $TG_2$ range reveals a frequency comb with the free spectral range $\Delta f_{sub} = 1/t_{r1} = 6.4$ MHz [cf. Figs. 3(c)–3(e)]. In order to understand the origin of the comb, we remind ourselves that the transmission through an ideal Bragg resonator with a cavity always approaches unity at the resonance frequency. The resonance modes of the surface and main acoustic cavities are thus expected to propagate through the whole structure. The constructive interference of BAWs after multiple round-trips results in the frequency comb—the phonon backfeeding effect. The quality factor of the comb resonances reaches values $Q_{a,A} \geq 2800$ at 6.937 GHz.

Figure 3(b) shows the corresponding results for the propagation of 20-GHz acoustic waves in sample $B$. The slightly shorter echo round-trip delays [cf. Fig. 2(c)] as compared to sample $A$ are attributed to a slightly smaller wafer thickness. Backtransformation of the time signal within the $TG_1$ and $TG_2$ regions to the frequency domain in Fig. 3(b) reveals the corresponding surface $f_S = 19.65$ GHz and cavity $f_{MC} = 20.97$ GHz acoustic resonances; cf. Fig. 3(d). The signatures associated with the $f_S$ mode are less pronounced than the corresponding ones for sample $A$ mainly due to the higher noise background levels in the 20-GHz range. Similar to the case of sample $A$, the interference of the reflected acoustic waves creates a frequency comb with $\Delta f_{sub} = 6.4$ MHz; cf. Fig. 3(j). Within the $f_{MC}$ range [around 20.97 GHz; cf. Fig. 3(i)], the comb resonances reach a quality factor of $Q_{c,B} = 6800$ (cf. Table I).

TABLE I. Measured [$Q_c$] and estimated [$Q_c$ (calc)] quality factors for the comb modes from Eqs. (1) and (2) using $d_s = \lambda_{BAW}$ and $\alpha_{eff} = 8 \times 10^{-4}$ $\mu$m$^{-1}$ [43]. $Q_{MC}$ is the bare quality factor of the acoustic mode determined from the envelope of the $s_{11}$ response of the BAWR. $Q_{sub}$ is the quality factor of the bare substrate determined from the BAW absorption coefficient $\alpha_{eff}$ [cf. Eq. (1)].

| Sample | $f_{BAW}$ (GHz) | $Q_{sub}$ | $Q_{MC}$ | $Q_c$ (calc) | $Q_c$ |
|---|---|---|---|---|---|
| $A$ | 7 | 3050 | 172 | 4100 | 2800 |
| $B$ | 20 | 8700 | 982 | 14500 | 6800 |

### D. Quality factor of the acoustic resonances

The quality factor $Q_c$ of the acoustic comb resonances is much larger than the bare quality factor of the MCs ($Q_{MC}$) determined by the acoustic reflection coefficient and losses in the MC spacer and the DBRs. Experimentally, $Q_{MC}$ can be quantified as the ratio between the center frequency and width of the $s_{11}$ envelopes (cf. Fig. 3; values for samples $A$ and $B$ are summarized in Table I). The previous section also shows that $Q_c$ increases for sample $B$, which has a higher acoustic frequency. From the values in the Table I, we determine a very large $Q_{c,A} \times f \sim 2 \times 10^{13}$ Hz product for the comb resonances around 6.94 GHz in sample $A$. Sample $B$ exhibits even higher $Q_{c,B} \times f \sim 1.4 \times 10^{14}$ Hz at 20 GHz. Interestingly, the ratio between the effective quality factors of the samples of $Q_{c,B}/Q_{c,A} = 2.4$ compares reasonably well with the ratio of $f_{MC,B}/f_{MC,A} = 3$ between their resonance frequencies, thus proving that this figure of merit does not reduce with increasing frequency. We show in this section that the enhancement of the quality factor arises from phonon backfeeding to the spacer region via reflections at the front and back surface of the sample.

In the following, we analyze the mechanisms determining the acoustic $Q$ factor in the samples including the role of phonon backfeeding. The propagation properties of SHF BAWs in GaAs (001) substrates at low temperatures have been studied in Ref. [43]. Here, the propagation losses are expressed in terms of an effective amplitude absorption coefficient $\alpha_{eff}$, which includes losses during both propagation and reflection at the sample boundaries.

Furthermore, Ref. [43] also reports that $\alpha_{\text{eff}}$ is essentially temperature independent below 20 K, where it becomes limited by reflection losses at the sample boundaries, which are only weakly frequency dependent between 5 and 20 GHz. The effective fraction of the acoustic power absorbed per round-trip across the substrate can then be written as $2r_b = 4\alpha_{\text{eff}} d_{\text{sub}}$, where $r_b$ is the power loss fraction per round-trip, and $d_{\text{sub}}$ denotes the substrate thickness. In this approximation, the $Q$ factor of the comb resonances in a bare GaAs substrate of thickness $d_{\text{sub}}$ can then be expressed as

$$Q_{\text{sub}} = 2\frac{d_{\text{sub}}}{r_b \lambda_{\text{BAW}}} = \frac{1}{2\alpha_{\text{eff}} \lambda_{\text{BAW}}}. \tag{1}$$

The above expression neglects BAW reabsorption by the BAWR. An important consequence of Eq. (1) is that, since $\alpha_{\text{eff}}$ remains constant between 5 and 20 GHz, $Q_{\text{sub}}$ is expected to increase with the BAW frequency.

The previous analysis can be extended to the MC structures if the acoustic losses at the high-quality MC interfaces can be neglected. In this case, the main effect of the MC is to increase the effective round-trip length by $Q_{\text{MC}} d_s$, where $d_s$ denotes the thickness of the MC spacer, and $Q_{\text{MC}}$ is the quality factor of the bare MC determined from the reflection coefficient of the DBRs (i.e., by neglecting BAW backfeeding due to reflections at the sample boundaries). The effective acoustic $Q$ for the comb resonances is obtained:

$$\begin{aligned} Q_c &= 2\frac{d_{\text{sub}} + d_s Q_{\text{MC}}}{r_b \lambda_{\text{BAW}}} \\ &= Q_{\text{sub}}\left(1 + \frac{d_s}{d_{\text{sub}}} Q_{\text{MC}}\right). \end{aligned} \tag{2}$$

The value of $Q_c$ approaches the quality factor $Q_{\text{sub}}$ of the bare substrate for $Q_{a,\text{MC}} \ll (d_{\text{sub}}/d_s)$, while for $Q_{a,\text{MC}} \gg (d_{\text{sub}}/d_s)$ there is a considerable enhancement of the quality factor due to acoustic confinement in the MC.

Table I compares the measured quality factors ($Q_c$) of the acoustic cavity modes in samples $A$ and $B$ with the values [$Q_c$ (calc)] estimated from Eqs. (1) and (2) assuming $d_s = \lambda_{\text{BAW}}$ and $\alpha_{\text{eff}} = 8 \times 10^{-4}$ $\mu\text{m}^{-1}$ [43]. The latter $Q_c$ value yields the quality factors $Q_{\text{sub}}$ for the bare substrate listed in the third column of the table. In general, the calculated $Q_c$'s overestimate the measured ones. This discrepancy may be due to the simplicity of the model, which neglects losses at the BAWR as well as at the MC interfaces. Nevertheless, the model accounts for the higher $Q_c$ for the 20-GHz MC, which is mainly due to the higher $Q_{\text{MC}}$ arising from the larger number of acoustic DBR stacks.

## III. PHONON-POLARITON INTERACTIONS IN HYBRID MICROCAVITIES

### A. Lateral field distribution in ring-shaped BAWR

The spectroscopic studies of the phonon-polariton interactions in the hybrid MCs require optical access to the sample area underneath the BAWRs, which is difficult in conventional BAWRs due to the opaque metal electrodes. In order to overcome this limitation, we use for the spectroscopic experiments special BAWRs with ring-shaped electrodes, as displayed in Fig. 1(a). In a typical PL experiment, the exciting laser light is focused at the center of a BAWR aperture. We show in this section that this electrode geometry not only provides optical access to the MC spacer but also enhances the phonon field within the illumination area.

The spatially resolved photoluminescence (PL) measurements are carried out in the 10- to 60-K temperature range in a cryogenic (liquid He) probe station. Optical excitation is provided by a pulsed diode laser emitting at 635 nm with average powers between 10 and 200 $\mu$W focused onto a 10-$\mu m^2$ spot. The exciting laser pulses have a repetition rate of 30 MHz and widths ($\gtrsim$100 ps) far exceeding the typical photon lifetimes in the MC (of approximately 2 ps for an optical quality factor $Q \sim 1000$). The PL is spectrally resolved using a single grating spectrometer with resolution of 100 $\mu$eV and detected by a liquid-nitrogen-cooled CCD detector. The typical PL acquisition times are between 1 and 30 s per spectrum.

We probe the lateral distribution of the BAW field within the BAWR aperture by exploiting the strong dependence of the QW excitonic energies on strain. The experiments are carried out at 50 K, where the excitonic resonances of sample $A$ are largely decoupled from the optical cavity resonance (see Appendix B). The experimental configuration is illustrated in the top-view micrograph of the BAWR of Fig. 4(a). Figure 4(b) displays a PL map obtained by exciting sample $A$ with the laser focused on the 6-$\mu$m-diameter spot at the center of the BAWR aperture and recording the PL emitted within the region delimited by the dashed lines in Fig. 4(a) with spatial resolution along $y$. The PL extends over a region much larger than the size of the laser spot due to diffusion and drift of the photoexcited excitons.

The map of Fig. 4(b) shows two well-defined excitonic peaks designated $X_1$ and $X_2$ corresponding to the two excitonic resonances arising from the tunnel coupling of the QWs in this sample (cf. Sec. II A). These features can be identified in the spectral cross section through the center of the aperture displayed in Fig. 4(d) (blue line). The blue-shifted broad peak $C$ is centered around the optical mode of the MC. The emission at this energy is attributed to the luminescence from (mainly carbon) defects in the substrate, which is resonant to the optical MC mode. The large spectral width (compared to the expected narrow optical transmission of the MC for normal incidence) results from the fact that the PL is collected using a high-NA objective.

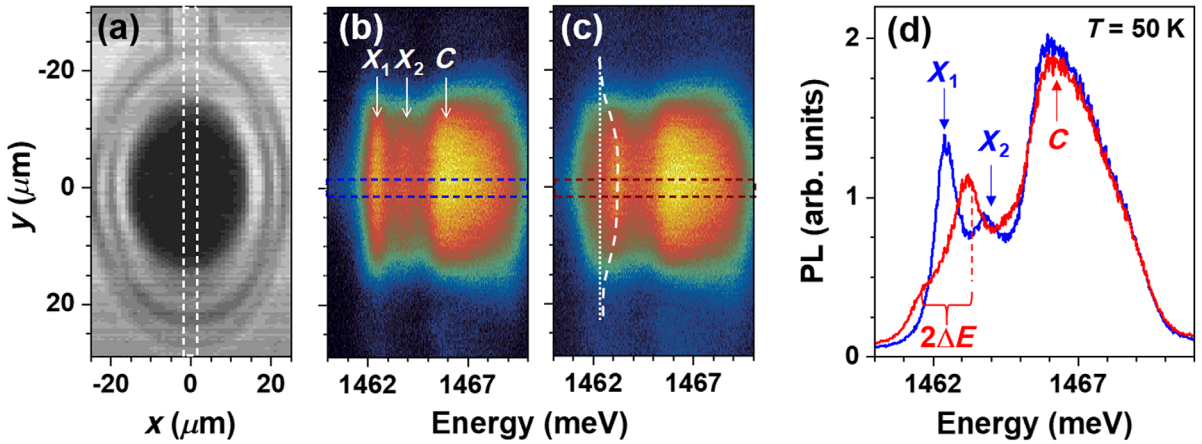


FIG. 4. (a) Optical micrograph of a ring-shaped BAWR. The vertical dashed lines delimit the surface imaged on the slit of the spectrograph for PL spectral analysis. (b),(c) Maps of PL intensity as a function of the energy (horizontal axis) and position along the slit (vertical axis) without (b) and under BAW excitation of the acoustic MC mode $f_{\mathrm{MC}} = 6.9247$ GHz and rf power $P_{\mathrm{rf}} = 14$ dBm (c). These maps are recorded by collecting the PL emitted within the dashed rectangle in (a), excited by the 635-nm laser focused at the center of the BAWR aperture. (d) Comparison of PL spectra recorded in the center of the BAWR aperture in the absence (blue) and in the presence of the BAW (red). The spectra are produced by spatial integration over the regions delimited by the horizontal dashed lines in (b) and (c), respectively. $\Delta E$ is the amplitude of the energy modulation of the excitonic resonances.

The spectroscopic measurements in the presence of a BAW are carried out using a special modulation technique to discriminate the BAW-induced changes from potential thermal effects induced by the rf power applied to the transducer [47] (see Appendix D for details). In short, we establish that the rf-induced heating does not play a significant role [47].

When the BAWR is driven at one of the comb resonances within the cavity acoustic mode ($f_{\mathrm{rf}} = 6.9247$ GHz), the energy and spatial characteristics of the PL maps are modified as shown in Fig. 4(c) and in the cross section spectrum of Fig. 4(d). Specifically, the sinusoidal modulation of the excitonic energies by the BAW strain field induces the apparent splitting of the PL line into a doublet separated by an energy splitting $2\Delta E$ in time-integrated PL spectra [48]. The doublet lines are indicated in Fig. 4(d). In the present case, the intensity of the higher-energy doublet is much larger than the lower-energy one: This behavior is attributed to the different coupling strengths of the doublet components to the photonic mode of the MC. While the intensity of the higher-energy doublet component increases as it approaches the photonic mode, the other one moves away, thus decreasing the coupling. A comparison with the corresponding spectrum recorded in the absence of the BAW [cf. Fig. 4(d)] reveals that the BAW effectively splits the $X_1$ peak by $2\Delta E \approx 1.5$ meV. The $X_2$ peak is affected in a similar manner. However, due to its relatively low intensity it merges with the shoulder of the $C$ peak. The splitting corresponds to the peak-to-peak amplitude of the strain-induced energy shifts. It is related to the amplitude $u_{zz,0}$ of the BAW strain field by

$$\Delta E = a_h \eta_s u_{zz,0}, \tag{3}$$

where $\eta_s u_{zz,0}$ is the strain modulation amplitude at the QW position, and $a_h \approx 10$ eV is the GaAs hydrostatic deformation potential for electron-hole transitions [49].

The curved shape of the $\Delta E$ splitting of the $X_1$ line in Fig. 4(c) (dashed line) clearly shows that the strain field increases toward the center of the aperture, thus indicating that the ring-shaped electrodes concentrate the acoustic field at the aperture center. The latter effect is attributed to the lateral propagation of modes excited underneath the ring-shaped electrodes. This result opens an interesting possibility of engineering acoustic in-plane gradients by the design of the electrodes' shape.

### B. Effect of BAW on polariton spectrum

We now turn our attention to the impact of the BAWs on the PL of the polariton modes of sample $A$. By lowering the temperature, the $X_1$ and $X_2$ excitonic resonances displayed in Fig. 4(d) blueshift and strongly couple to the (relatively temperature insensitive) $C$ cavity resonance. As a result, three polariton branches with characteristic parabolic dispersion are observed at 10 K (cf. Appendix B). Fitting the dispersion using the three coupled oscillators model yields the Rabi splitting energy of approx. $\Omega_{\mathrm{Rabi}} = 2$ meV.

The color map of Fig. 5(a) shows the time-integrated polariton PL as a function of the rf frequency ($f_{\mathrm{rf}}$) applied to the BAWR. The PL maps in Figs. 5(a) and 5(c) are obtained by sweeping the $f_{\mathrm{rf}}$ over a wide frequency range with a small frequency step and recording, for each step, a PL spectrum [similar to the one in Fig. 4(d), red curve]. The BAW induces an energy modulation of amplitude $\Delta E$ as well as changes in PL intensity, which are very pronounced at the comb resonances. Figure 5(b) compares the measured amplitude $\Delta E$ of the energy shifts in Fig. 5(a) with the

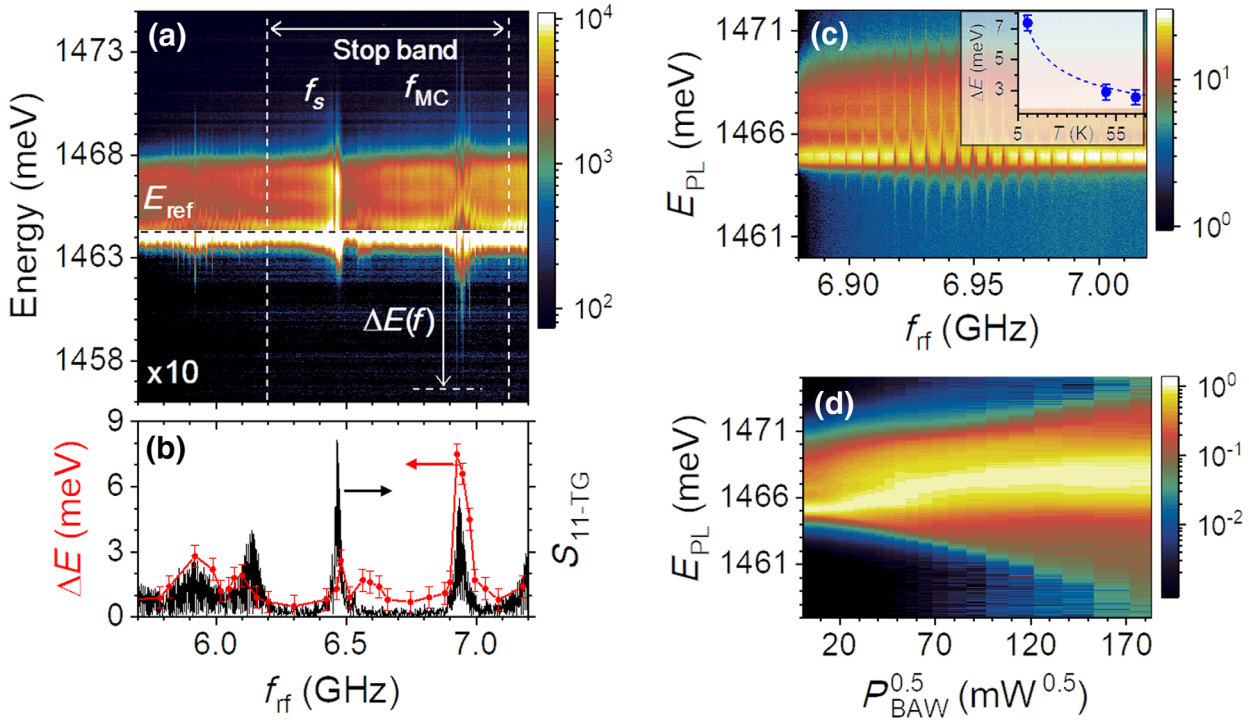


FIG. 5. Polariton-phonon interaction in a hybrid microcavity. (a) Spectral dependence of the photoluminescence on the rf frequency for sample *A* recorded at 10 K and the nominal rf power of 24 dBm. The acoustic stop-band limits are indicated by the vertical dashed lines. (b) Comparison of the time-gated $s_{11}$ parameter of a similar device with the acoustically induced energy modulation amplitude of the comb resonances $\Delta E(f)$ calculated with respect to the $E_{ref} = 1464.3$ meV [indicated in (a) with the horizontal black dashed line]. (c) The rf-frequency dependence of the PL recorded for a fixed rf power $P_{rf} = 14$ dBm applied to the BAWR at 10 K corresponding the coupled linear power amplitude $P^{0.5}_{BAW} = 45$ mW$^{0.5}$ showing the effects of the frequency comb with $\Delta f_{sub} = 6.4$ MHz. The inset displays the temperature ($T$) dependence of the energy modulation amplitude $\Delta E$. The dashed line in the inset is a guide to the eye. (d) Dependence of the PL recorded for a fixed rf frequency $f_{rf} = 6.9312$ GHz applied to the BAWR at 10 K on $P^{0.5}_{BAW}$.

electrical response $s_{11,TG}$ showing an excellent correlation with the comb resonances in $s_{11,TG}$. Moreover, the highest modulation amplitudes $\Delta E$ are found at the MC resonance $f_{MC}$, where the acoustic field becomes confined within the spacer, thus increasing the interaction with the QW excitons. Note, however, that weaker modulation is also observed outside of the acoustic stop band.

Figure 5(c) displays an enlargement of the spectral PL map around $f_{MC}$. The sharp PL comb resonances have an effective quality factor comparable to the one determined from the $s_{11,TG}$ curves of Fig. 3(b). The PL energy shift reaches amplitudes up to $\Delta E = 8$ meV, which exceed several times the value of $\Omega_{Rabi}$. Furthermore, Fig. 5(d) shows the dependence of the $\Delta E$ for a fixed comb frequency on the rf power applied to the BAWR.

The large energy modulation at the comb frequencies in comparison to the Rabi splitting in Fig. 5 leads to a complex dependence of the PL intensity on energy. It can be understood by taking into account that the undisturbed polaritons are slightly positively detuned (i.e., with the excitonic levels redshifted with respect to the cavity photons) and that the BAW strain field mainly modulates the excitonic energies. The PL intensity thus reduces significantly when the BAW redshifts the excitonic lines. In contrast, when the excitonic energies are blueshifted, the emission initially increases as the resonances approach the photonic mode and then decreases for higher energy shifts. Finally, we note that the PL emission reduces below the detection limit for large energy shifts. Therefore, the shifts $\Delta E$ measured in these plots represent the lower bound to the energy modulation amplitude of the excitonic states.

We conclude this section with a comparison between the polariton modulation amplitudes induced by electrically excited acoustic waves with the corresponding values reported for strain transients excited by ps laser pulses. The ps-acoustics studies of (Al,Ga)As polariton MCs with an $In_{0.04}Ga_{0.96}As$ QW of Ref. [40] quoted small (sub-meV) energy modulation amplitudes. A subsequent study by the same group reported the observation of phonon sidebands due to the nonadiabatic energy shifts of the polariton lines with amplitudes up to 2 meV [41]. According to the authors, the strong THz strain pulses shift the excitonic energies by as much 10 meV: These huge shifts cannot be spectrally detected because they are accompanied by a strong reduction of the oscillation strength [42]. The optically induced strain transients are excited by laser

sources with per pulse powers typically in the kW to MW range [21,40]. Here, in contrast, we report polariton energy shifts of comparable amplitudes (up to 8 meV) induced by standing strain fields generated using a much lower electrical power (of approximately 0.3 W). The latter reduction becomes possible due to the coherent (and continuous) nature of the electrically excited waves, which enables field buildup via the backfeeding effect.

### C. BAW modulations mechanisms

In order to understand the mechanisms responsible for the phonon-induced modulation of polariton energies, we compare in Figs. 6(a)–6(c) time-averaged PL spectra of sample $A$ recorded at different temperatures in the absence of acoustic excitation (thin blue lines) with the ones acquired under the excitation at a comb frequency in the $f_{MC}$ range (thick red lines). Similar to the behavior previously discussed in connection with Fig. 4(d), the excitonic states of this sample at temperatures above 50 K are redshifted and only weakly coupled to the cavity resonance ($C$), giving rise to the three PL peaks in Figs. 6(a) and 6(b). When the BAW is turned on [red curves in Figs. 6(a) and 6(b)], the sinusoidal modulation of the excitonic energies with amplitude $\Delta E$ leads to two shoulders in the time-averaged PL spectra shifted by $\pm\Delta E$ with respect to the unperturbed excitonic energy indicated by the dotted vertical blue lines [48]. As in Fig. 4(d), the redshifted shoulder is much weaker than the blueshifted one (dotted vertical red lines) due to the large detuning with respect to the photonic resonance. More importantly, the photonic mode ($C$ at 1465 meV) remains essentially unperturbed, thus proving that the energy modulation is dominated by the strain-induced modulation of the excitonic resonances via the deformation potential mechanism quantified by Eq. (3).

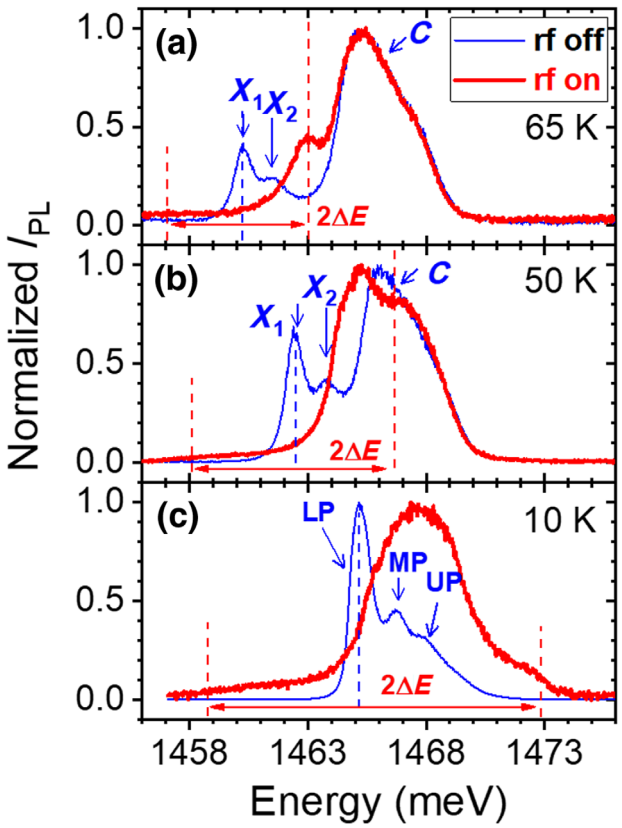


FIG. 6. Modulation of polaritons by MC acoustic modes. Time-averaged PL spectra of sample $A$ recorded in the absence (thin blue lines) and in the presence (thick red lines) of a BAW with frequency $f_{BAW} = 6.931$ GHz recorded at (a) 65, (b) 50, and (c) 10 K. $\Delta E$ denotes the energy modulation amplitude of the excitonic levels in (a) and (b), and polariton states in (c).

At lower temperatures, the excitonic lines blueshift, and the strong coupling to the photonic mode leads to the formation of the lower- (LP), middle- (MP), and upper- (UP) polariton states indicated in Fig. 6(c). The acoustic modulation induces a large dynamical modulation of the polariton spectrum resulting in the appearance of redshifted and blueshifted shoulders shifted by $\Delta E \approx 8$ meV with respect to the LP peak energy [dotted vertical lines in Fig. 6(c)]. The BAW-induced energy modulation in Fig. 6(c) is sufficiently large to considerably change the exciton and photon fractions of the respective polariton branches. Specifically, when the dynamic detuning reaches the large positive value of $\Delta = C - X_1 \approx 8$ meV, the LP polariton is essentially excitonlike. From the $\Delta E$ value in Fig. 6(c), we obtain using Eq. (3) a strain amplitude at the QW positions of $\eta_s u_{zz,0} = 8 \times 10^{-4}$. Since the amplitude of the phonon displacement field $u_{z,0}\hat{z}$ is given by $u_{z,0} = (\lambda_a/2\pi)u_{zz,0}$, the effective optomechanical coupling is estimated to be $g_{\text{eff}} = \Delta E/u_{z,0} = (\eta_s 2\pi/\lambda_a)a_h = 18$ THz/nm.

Finally, another interesting feature of the BAW modulation is the strong reduction of $\Delta E$ with increasing temperature illustrated in the inset of Fig. 5(c). The latter effect is attributed to the increased acoustic propagation losses in GaAs for temperatures above 20 K [50]. Indeed, according to Eq. (7) of Ref. [43], the effective acoustic absorption coefficient $\alpha_{\text{eff}}$ doubles when the temperature increases from 10 to 65 K. Since the amplitude of the acoustic field scales with $1/\alpha_{\text{eff}}$, the increased absorption correlates well with the 2 times reduction of $\Delta E$ (from 8 to 3.5 meV) from 10 to 65 K displayed in the inset of Fig. 5(c).

### D. Hybrid microcavities for 20-GHz phonons

SHF phonons in hybrid MCs open interesting possibilities for quantum optoacoustics as well as for the time-coherent manipulation of polaritons. In particular, the energy quantum of 20-GHz phonons of 80 $\mu$eV can exceed several times the linewidth of polariton BEC condensates in similar samples [51,52]. Thus, the demonstration of energy modulation amplitudes larger than the polariton linewidths at these frequencies constitutes an important milestone to

reach the nonadiabatic, sideband-resolved modulation regime. As the effective phonon absorption losses at low temperatures remain approximately constant in the (3–30)-GHz frequency range, the hybrid MC platform allows a straightforward increase of the effective $Q_a$ by increasing the frequency [43]. In this section, we show experimental results for polariton modulation in sample $B$, which confines 20-GHz phonons with a $Q_{c,B} = 6800$.

The polariton states in sample $B$ arise from the strong coupling of MC photons to excitons in single QW (cf. Appendix C). Figure 7(a) displays a PL map recorded while driving the BAWR across the $f_{\mathrm{MC}}$ frequency range (19.92–19.97 GHz). Similar to the behavior of sample $A$ [cf. Fig. 5(c)], the BAW induces a comb of resonances in the PL spectrum with energy modulation of the lower-polariton energies reaching amplitudes $\Delta E$ up to 2 meV [cf. Fig. 7(b)]. The lower modulation amplitudes as compared to sample $A$ are attributed to the lower strain amplitudes due to the weaker electroacoustic conversion efficiency of the BAWR at 20 GHz. The weaker modulation of the upper-polariton branch in sample $B$ is attributed to its mostly photonic character. The $\Delta E$ values yield using Eq. (3) strain amplitudes $\eta_s u_{zz,0} \approx 1 \times 10^{-4}$ and $g_{\mathrm{eff}} = 50$ THz/nm at 20 GHz.

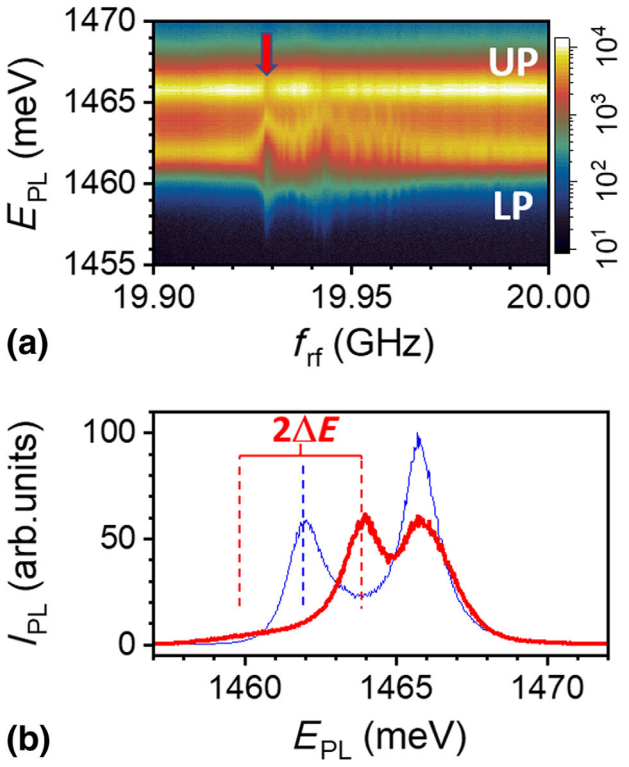


FIG. 7. Optomechanical response of a hybrid MC for 20-GHz BAWs. (a) The rf-frequency dependence of the PL recorded for a fixed rf power $P_{\mathrm{rf}} = 24$ dBm applied to the BAWR displaying the effect of the BAW on the PL emission. The red arrow points at one of the acoustic resonances. The LP and UP stand for the lower-polariton branch and the upper-polariton branch, respectively. (b) Time-averaged PL spectra recorded at 10 K in the absence (thin blue line) and presence (thick red line) of a BAW with frequency $f_{\mathrm{BAW}} = 19.926$ GHz [cf. red arrow in (a)]. The measurements are carried out at 10 K.

## IV. CONCLUSION AND PROSPECTS

We introduce a novel platform for electrically driven exciton-polariton optomechanics at 20 GHz based on the coupling of polaritons and electrically generated BAWs confined in a planar MC. On the one hand, the platform profits from the long effective lifetimes of phonons confined in the spacer region of the MC. These MCs are less susceptible to the degradation of the acoustic quality factor, for example, due to the surface defects. As a consequence, the values of $Q_a \times f$ products in the SHF range exceed $10^{14}$ Hz and are comparable to the highest values reported for much lower vibration frequencies [1,43,53]. On the other hand, the platform exploits the high sensitivity of the excitonic resonances to confined strain fields, which enables the modulation amplitudes of the polariton energies far exceeding the light-matter coupling strength as well as effective optomechanical couplings in the $g_{\mathrm{eff}} \sim 50$ THz/nm range. The results thus demonstrate electrically driven modulation of optical signals at 20 GHz, which, when combined with the nonlinear character of polaritons (e.g., BEC), can be exploited for the on-demand generation of coherent ps optical pulses from semiconductor structures.

The work opens the way to resonant optomechanics in the nonadiabatic, resolved sideband regime using polariton condensates with spectral linewidths considerably smaller than the inverse phonon frequency (and, thus, much narrower than the ones in the subcondensation regime reported here). The latter condition enables the study and electrical control of advanced phenomena such as mechanical self-oscillations and phonon lasing [52]. Finally, recent developments in MC structures have demonstrated the feasibility of zero-dimensional confinement of polaritons [54,55] and phonons [56] in structured MCs. Electrically driven high-frequency BAWs in these structures enable access to the single-phonon regime at temperatures (of approximately 1 K) substantially larger than for sub-GHz vibrations.

The demonstrated platform offers a road to electrically driven optomechanical lattices and nonlinear phononics (akin to nonlinear optics) with structured hybrid MCs. In these structures, polaritons are laterally confined in $\mu$m-sized traps defined by etched pillars [57] or by intracavity traps created by the etching and overgrowth technique [55,58]. These traps also laterally confine (10–100)-GHz phonons [56]. On the one hand, the electrical generation of a large density of confined phonons can enable nonlinear acoustic processes, e.g., harmonics generation [59], frequency mixing, parametric oscillations, and parametric amplification. On the other hand, similar to polaritons [60], in-plane phonon molecules and lattices can be

realized by a proper lateral arrangement of traps. Such 1D/2D phononic crystals [61] are particularly interesting for the investigation of collective nonlinear phonon dynamics, topology, and tunable band structure. They may form the basis for applications in arrays of sensors, clocks, and synchronization devices as well as for the realization of materials with engineered heat conductivity.

## ACKNOWLEDGMENTS

We thank Dr. Timur Flissikowski for discussions and for a critical review of the manuscript. We also acknowledge the technical support from R. Baumann, S. Rauwerdink, and A. Tahraoui in the sample fabrication process. We acknowledge financial support from the German DFG (Grant No. 359162958), the QuantERA grant Interpol [EU-BMBF (Germany) Grant No. 13N14783], and FAPESP (Brazil, Grant No. 2017/24311-6).

## APPENDIX A: FIELD DISTRIBUTION IN HYBRID MICROCAVITIES

As we show in the main text, the modulation of the QW excitonic levels by the strain field $u_{zz} = \partial u/\partial z$ of the BAW is the dominating mechanism determining the optomechanical coupling in these structures. Here, $\mathbf{u} = (0, 0, u_z)$ is the BAW displacement field as a function of the $z$ coordinate perpendicular to the MC surface. Optimization of this coupling requires, therefore, that the QWs embedded in the MC spacer are placed close to the antinodes of both the optical and the acoustic strain fields.

It turns out that the requirement stated above can never be fully satisfied. In $Al_xGa_{1-x}As$ alloys, the coincident ratio between the light and sound velocities as well as between the inverse acoustic impedance is approximately independent of the composition $x$ also implies that the antinodes of the acoustic ($u_z$) and optical field ($F_x$ assumed to be polarized along the surface direction $x$) occur at the same $z$ coordinate [14]. The antinodes of $u_z$ are, however, nodes of $u_{zz}$, thus implying a vanishing modulation of the excitonic energy.

Fortunately, a very good position matching of the maxima of $u_{zz}$ and $F_x$ can still be achieved in the hybrid MC of sample $A$ by slightly displacing the QWs with respect to the antinodes of $u_{zz}$. Figures 8(b) and 8(d) show calculations of the optical ($F_x$) and acoustic ($u_{zz}$) field distributions within the spacer of the MC [cf. Fig. 8(a)] carried out using a transfer-matrix approach. Figure 8(c) shows, for reference, the depth modulation of refractive index $n$ in the same regions indicating the position of the QWs. These plots show that the antinodes of $u_{zz}$ coincide with the nodes of $F_x$. Note that the separation between the QWs is much smaller than the wavelength of both the optical and acoustic fields, so that they can be considered to be subjected to an approximately constant field amplitude. The middle $z$ coordinate of the two QWs is slightly shifted away from the antinode of $u_{zz}$ to match an antinode of $F_x$. The strain field at the QWs is still about $\eta_s = 80\%$ of its maximum value, so that the small shift only marginally reduces the optoelectronic coupling.

A similar approach is used in sample $B$: This sample contains a single (In,Ga)As QW, which is slightly displaced from the antinodes of the optical field to ensure a higher coupling to the acoustic field.

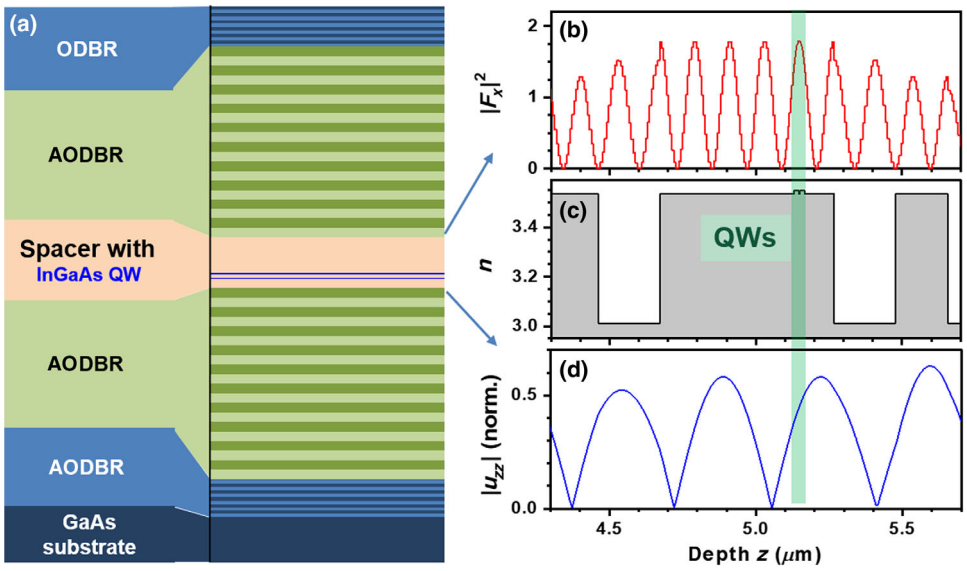


FIG. 8. (a) Layer structure of the hybrid microcavity (sample $A$). Depth profiles within the spacer region of the hybrid microcavity of the (b) optical field $F_x$ at the photonic resonance energy, where $x$ is the polarization direction on the MC surface, (c) refractive index, $n$, and (d) normalized acoustic strain field $u_{zz}$ for the acoustic resonance frequency $f_{MC} = 6.9$ GHz. The green band designates depth of the two QWs.

## APPENDIX B: TEMPERATURE DEPENDENCE OF THE OPTOELECTRONIC RESONANCES

The nature of the light-matter coupling in the MCs can be accessed by studying the energy dispersion of the photonic and excitonic resonances obtained from angle-resolved PL spectra. Typical dispersion plots are displayed in Figs. 9(b)–9(e) for different temperatures. The momentum-resolved maps of Fig. 9 are measured by positioning the entrance slit of a single-pass spectrometer in a plane conjugate to the Fourier (back focal) plane of the objective lens. At temperatures above 50 K [i.e., Figs. 9(d) and 9(e)], the photonic resonance shows a parabolic dispersion, which contrasts with the essentially flat dispersions of the redshifted excitonic states. This behavior is typical for excitonic resonances in the regime of the weak coupling to photonic modes. It is interesting to note the presence of two excitonic lines: a main line denoted as $X_1$ and a weaker one ($X_2$) blueshifted by approximately 1.5 meV. The appearance of two lines is presently not fully understood. Two InGaAs QWs in this sample are (unintentionally) tunnel coupled by a thin (5-nm-thick) GaAs barrier. This coupling produces excitonic bonding and antibonding resonances split by approximately 4.5 meV, which is larger than the energy difference of approximately 2 meV between the $X_1$ and $X_2$ lines in Fig. 9(e).

An alternative explanation is that one of the lines corresponds to the free exciton ($X_2$) and the second to a trion state ($X_1$) resulting from the coupling of an exciton to a residual charge in the QWs. For the subsequent discussions (here and in the main text), the important point is that both lines are of excitonic nature.

As the temperature reduces, the excitonic resonances blueshift and strongly couple to the photonic mode, giving rise to the LP, MP, and UP polariton branches indicated in Fig. 9(a). By fitting the angular-resolved PL map at 10 K to a model of three coupled resonances, we obtain a light-matter Rabi splitting $\Omega_{\mathrm{Rabi}} = 2 \pm 0.3$ meV.

## APPENDIX C: POLARITON SPECTRUM IN SAMPLE *B*

Figure 10 shows the spatial dispersion of emission of sample $B$; the "0" of the horizontal axis corresponds to the wafer center. Typical anticrossing behavior of the cavity mode ($C$) and the exciton resonance ($X$) is observed. The fitting of the experimental data with the two coupled-oscillators model yield Rabi splitting $\Omega_{\mathrm{Rabi}} = 3 \pm 0.5$ meV. The measurements of Fig. 7 are taken at $y \neq 7$ mm. At this position, the UP is photonlike, while the LP is excitonlike.

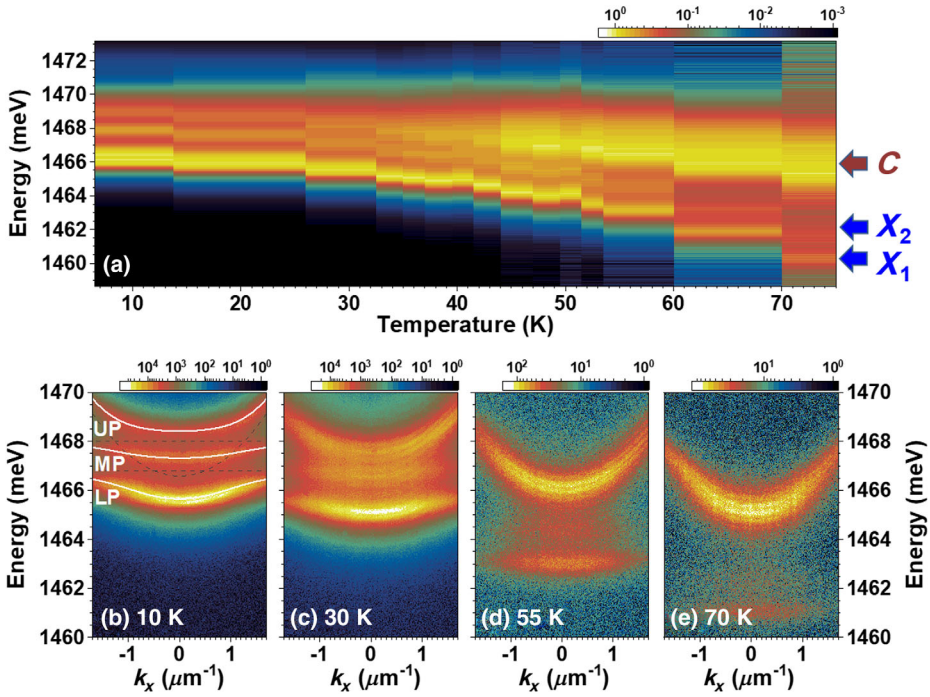


FIG. 9. Temperature dependence of the PL of the hybrid MC (sample $A$). (a) Temperature dependence of the PL spectrum. $X_1$ and $X_2$ are excitonic resonances of the coupled InGaAs QWs, which couple to the photonic ($C$) mode of the MC to form the lower (LP), middle (MP), and upper (UP) states at low temperatures. Momentum-resolved PL at (b) 10, (c) 30, (d) 55, and (e) 70 K. Below 50 K, the system is in the strong-coupling regime. The solid lines in (e) are three coupled oscillator fits to the data. The dashed lines are bare energies. The fitted Rabi splitting energy is $\Omega_{\mathrm{Rabi}} = 2 \pm 0.3$ meV.

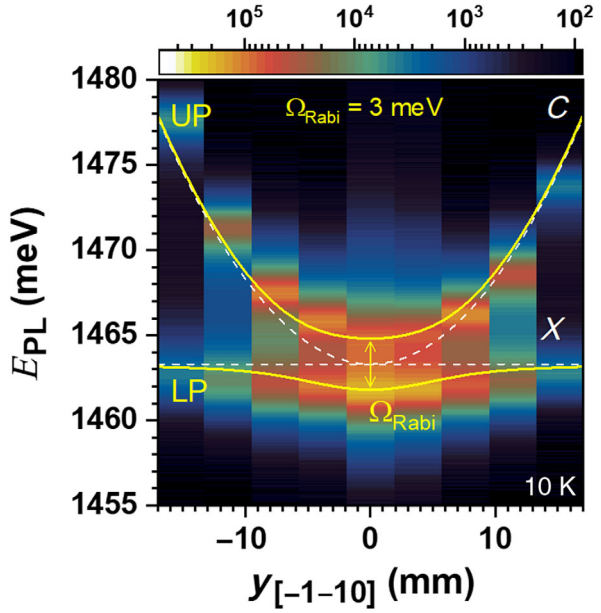


FIG. 10. Spatial dispersion of photoluminescence of sample $B$ at 10 K. The white dashed lines represent calculated spatial dispersion of bare cavity ($C$) and exciton ($X$) modes. The solid yellow lines are fits using the two coupled oscillators model. The fitted Rabi splitting energy is $\Omega_{\mathrm{Rabi}} = 3 \pm 0.5$ meV.

## APPENDIX D: COMPENSATION FOR THERMAL EFFECTS IN THE SPECTROSCOPIC MEASUREMENTS

The rf excitation of the transducers induces sample heating. The $s_{11}$ coefficient for the device [cf. in Fig. 2(a)] shows that at $f_{\mathrm{MC}} \approx 6.9$ GHz only about 12% of the applied rf power is converted into coherent phonons, and 88% are losses, including heating. Since the temperature sensor in the measurement setup is not placed directly on the sample, it cannot detect these changes. Alternatively, PL measurements allow us to probe the temperature locally, because the emission intensity and energy of the exciton depend strongly on the temperature. Figure 9(a) shows that we can detect temperature changes with an accuracy of 5 K.

In order to discriminate possible thermal effects arising from sample heating from the ones due to the coherent modulation by the BAWs, the acoustic PL measurements are carried out in the following way [47]. The rf generator and the pulsed semiconductor laser diode exciting the PL are triggered by a train of low-frequency square pulses (with frequencies between 1 and 10 kHz). To rule out the effect of the temperature, the measurements are carried out under two configurations for the relative phases between the pulse trains: (i) the in-phase condition, where the rf and optical excitation are present at the same time and (ii) out-of-phase condition—no temporal overlap between the rf and optical pulses. Because of the high pulse frequency, the sample temperature is the same for the two situations. Thus, the out-of-phase condition contains information about thermal phonons (heat). This method allows us to rule out the temperature contribution to the PL modulation shown in Fig. 4.

Figure 11 compares the PL spectra of a device with rf off, rf in phase, and rf out of phase (see Appendix D). The in phase and out of phase are measured at the same resonant rf frequency of 6.944 GHz and the same applied rf power of 14 dBm. Thus, the out-of-phase spectrum contains information about thermal phonons (heat). A comparison of the rf off and rf out of phase shows that the effect of the heating is negligible compared to the strain-induced modulation. For completeness, the green curve shows a PL spectrum recorded for the rf in-phase condition, which proves that the changes induced by the acoustic modulation are completely different from the purely thermal ones.

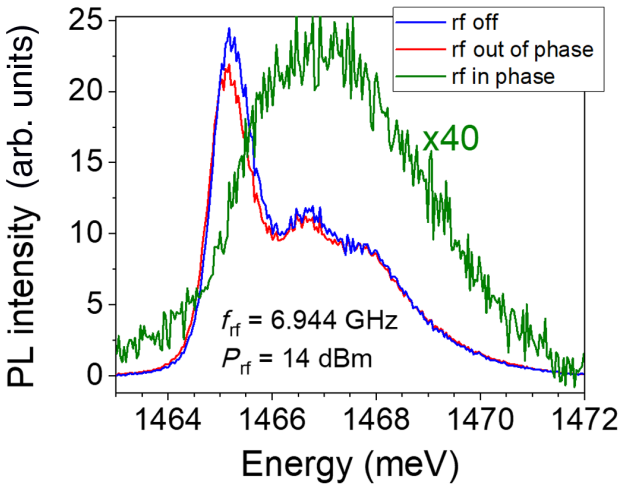


FIG. 11. (a) Comparison of the PL under three different rf conditions: (i) rf off, (ii) rf out of phase, and (iii) rf in phase. The in phase and out of phase are measured at the same resonant rf frequency 6.944 GHz and the same applied rf power 14 dBm.

[1] M. Aspelmeyer, T. J. Kippenberg, and F. Marquardt, *Cavity Optomechanics*, Rev. Mod. Phys. **86**, 1391 (2014).
[2] V. B. Braginsky, S. E. Strigin, and S. P. Vyatchanin, *Parametric Oscillatory Instability in Fabry-Perot Interferometer*, Phys. Lett. A **287**, 331 (2001).
[3] T. J. Kippenberg, H. Rokhsari, T. Carmon, A. Scherer, and K. J. Vahala, *Analysis of Radiation-Pressure Induced Mechanical Oscillation of an Optical Microcavity*, Phys. Rev. Lett. **95**, 033901 (2005).
[4] S. Groblacher, K. Hammerer, M. R. Vanner, and M. Aspelmeyer, *Observation of Strong Coupling between a Micromechanical Resonator and an Optical Cavity Field*, Nature (London) **460**, 724 (2009).
[5] J. Chan, T. P. M. Alegre, A. H. Safavi-Naeini, J. T. Hill, A. Krause, S. Groblacher, M. Aspelmeyer, and O. Painter, *Laser Cooling of a Nanomechanical Oscillator into Its Quantum Ground State*, Nature (London) **478**, 89 (2011).

[6] E. Verhagen, S. Deléglise, S. Weis, A. Schliesser, and T. J. Kippenberg, *Quantum-Coherent Coupling of a Mechanical Oscillator to an Optical Cavity Mode*, Nature (London) **482**, 63 (2012).
[7] S. Weis, R. Rivière, S. Deléglise, E. Gavartin, O. Arcizet, A. Schliesser, and T. J. Kippenberg, *Optomechanically Induced Transparency*, Science **330**, 1520 (2010).
[8] M. Gustafsson, P. V. Santos, G. Johansson, and P. Delsing, *Local Probing of Propagating Acoustic Waves in a Gigahertz Echo Chamber*, Nat. Phys. **8**, 338 (2012).
[9] T. Aref, P. Delsing, M. K. Ekström, A. F. Kockum, M. V. Gustafsson, G. Johansson, P. J. Leek, E. Magnusson, and R. Manenti, in *Superconducting Devices in Quantum Optics*, edited by R. H. Hadfield and G. Johansson (Springer International Publishing, Cham, 2016), pp. 217–244.
[10] S. Castelletto and A. Boretti, *Silicon Carbide Color Centers for Quantum Applications*, J. Phys. Photonics **2**, 022001 (2020).
[11] P. Kharel, G. I. Harris, E. A. Kittlaus, W. H. Renninger, N. T. Otterstrom, J. G. E. Harris, and P. T. Rakich, *High-Frequency Cavity Optomechanics Using Bulk Acoustic Phonons*, Sci. Adv. **5**, eaav0582 (2019).
[12] M. Trigo, A. Bruchhausen, A. Fainstein, B. Jusserand, and V. Thierry-Mieg, *Confinement of Acoustical Vibrations in a Semiconductor Planar Phonon Cavity*, Phys. Rev. Lett. **89**, 227402 (2002).
[13] A. Fainstein, B. Jusserand, and V. Thierry-Mieg, *Raman Scattering Enhancement by Optical Confinement in a Semiconductor Planar Microcavity*, Phys. Rev. Lett. **75**, 3764 (1995).
[14] A. Fainstein, N. D. Lanzillotti-Kimura, B. Jusserand, and B. Perrin, *Strong Optical-Mechanical Coupling in a Vertical GaAs/AlAs Microcavity for Subterahertz Phonons and Near-Infrared Light*, Phys. Rev. Lett. **110**, 037403 (2013).
[15] V. Villafane, S. Anguiano, A. E. Bruchhausen, G. Rozas, J. Bloch, C. G. Carbonell, A. Lemaitre, and A. Fainstein, *Quantum Well Photoelastic Comb for Ultra-High Frequency Cavity Optomechanics*, Quantum Sci. Technol. **4**, 014011 (2019).
[16] C. Thomsen, H. T. Grahn, H. J. Maris, and J. Tauc, *Surface Generation and Detection of Phonons by Picosecond Light Pulses*, Phys. Rev. B **34**, 4129 (1986).
[17] A. Bartels, T. Dekorsy, H. Kurz, and K. Köhler, *Coherent Zone-Folded Longitudinal Acoustic Phonons in Semiconductor Superlattices: Excitation and Detection*, Phys. Rev. Lett. **82**, 1044 (1999).
[18] A. Huynh, N. D. Lanzillotti-Kimura, B. Jusserand, B. Perrin, A. Fainstein, M. F. Pascual-Winter, E. Peronne, and A. Lemaître, *Subterahertz Phonon Dynamics in Acoustic Nanocavities*, Phys. Rev. Lett. **97**, 115502 (2006).
[19] M. F. P. Winter, G. Rozas, A. Fainstein, B. Jusserand, B. Perrin, A. Huynh, P. O. Vaccaro, and S. Saravanan, *Selective Optical Generation of Coherent Acoustic Nanocavity Modes*, Phys. Rev. Lett. **98**, 265501 (2007).
[20] A. A. Maznev, F. Hofmann, A. Jandl, K. Esfarjani, M. T. Bulsara, E. A. Fitzgerald, G. Chen, and K. A. Nelson, *Lifetime of Sub-THz Coherent Acoustic Phonons in a GaAs-AlAs Superlattice*, Appl. Phys. Lett. **102**, 041901 (2013).
[21] A. V. Scherbakov, P. J. S. van Capel, A. V. Akimov, J. I. Dijkhuis, D. R. Yakovlev, T. Berstermann, and M. Bayer, *Chirping of an Optical Transition by an Ultrafast Acoustic Soliton Train in a Semiconductor Quantum Well*, Phys. Rev. Lett. **99**, 057402 (2007).
[22] C. Brüggemann, A. V. Akimov, A. V. Scherbakov, M. Bombeck, C. Schneider, S. Höfling, A. Forchel, D. R. Yakovlev, and M. Bayer, *Laser Mode Feeding by Shaking Quantum Dots in a Planar Microcavity*, Nat. Photonics **6**, 30 (2012).
[23] T. Czerniuk, C. Brüggemann, J. Tepper, S. Brodbeck, C. Schneider, M. Kamp, S. Höfling, B. A. Glavin, D. R. Yakovlev, A. V. Akimov, and M. Bayer, *Lasing from Active Optomechanical Resonators*, Nat. Commun. **5**, 4038 (2014).
[24] T. Czerniuk, D. Wigger, A. V. Akimov, C. Schneider, M. Kamp, S. Höfling, D. R. Yakovlev, T. Kuhn, D. E. Reiter, and M. Bayer, *Picosecond Control of Quantum Dot Laser Emission by Coherent Phonons*, Phys. Rev. Lett. **118**, 133901 (2017).
[25] C. Weisbuch, M. Nishioka, A. Ishikawa, and Y. Arakawa, *Observation of the Coupled Exciton-Photon Mode Splitting in a Semiconductor Quantum Microcavity*, Phys. Rev. Lett. **69**, 3314 (1992).
[26] J. Kasprzak, M. Richard, S. Kundermann, A. Baas, P. Jeambrun, J. M. J. Keeling, F. M. Marchetti, M. H. Szymańska, R. André, J. L. Staehli, V. Savona, P. B. Littlewood, B. Deveaud, and L. S. Dang, *Bose-Einstein Condensation of Exciton Polaritons*, Nature (London) **443**, 409 (2006).
[27] A. Amo, D. B. D. Sanvitto, F. Laussy, E. del Valle, M. Martin, A. Lemaître, J. Bloch, D. Krizhanovskii, M. Skolnick, C. Tejedor, and L. Vina, *Collective Fluid Dynamics of a Polariton Condensate in a Semiconductor Microcavity*, Nature (London) **457**, 291 (2009).
[28] A. Baas, J. Karr, M. Romanelli, A. Bramati, and E. Giacobino, *Optical Bistability in Semiconductor Microcavities in the Nondegenerate Parametric Oscillation Regime: Analogy with the Optical Parametric Oscillator*, Phys. Rev. B **70**, 161307(R) (2004).
[29] S. Klembt, T. H. Harder, O. A. Egorov, K. Winkler, R. Ge, M. A. Bandres, M. Emmerling, L. Worschech, T. C. H. Liew, M. Segev, C. Schneider, and S. Höfling, *Exciton-Polariton Topological Insulator*, Nature (London) **562**, 552 (2018).
[30] Á. Cuevas, J. C. L. Carreño, B. Silva, M. De Giorgi, D. G. Suárez-Forero, C. S. Muñoz, A. Fieramosca, F. Cardano, L. Marrucci, V. Tasco, G. Biasiol, E. del Valle, L. Dominici, D. Ballarini, G. Gigli, P. Mataloni, F. P. Laussy, F. Sciarrino, and D. Sanvitto, *First Observation of the Quantized Exciton-Polariton Field and Effect of Interactions on a Single Polariton*, Sci. Adv. **4**, eaao6814 (2018).
[31] A. Delteil, T. Fink, A. Schade, S. Höfling, C. Schneider, and A. Imamoğlu, *Towards Polariton Blockade of Confined Exciton-Polaritons*, Nat. Mater. **18**, 219 (2019).
[32] D. Sanvitto and S. Kena-Cohen, *The Road Towards Polaritonic Devices*, Nat. Mater. **15**, 1061 (2016).
[33] S. Ghosh and T. C. H. Liew, *Quantum Computing with Exciton-Polariton Condensates*, npj Quantum Inf. **6**, 16 (2020).

[34] M. M. de Lima, Jr. and P. V. Santos, *Modulation of Photonic Structures by Surface Acoustic Waves*, Rep. Prog. Phys. **68**, 1639 (2005).

[35] B. Jusserand, A. N. Poddubny, A. V. Poshakinskiy, A. Fainstein, and A. Lemaitre, *Polariton Resonances for Ultrastrong Coupling Cavity Optomechanics in* GaAs/AlAs *Multiple Quantum Wells*, Phys. Rev. Lett. **115**, 267402 (2015).

[36] B. Jusserand, A. Fainstein, R. Ferreira, S. Majrab, and A. Lemaitre, *Dispersion and Damping of Multiple Quantum-Well Polaritons from Resonant Brillouin Scattering by Folded Acoustic Modes*, Phys. Rev. B **85**, 041302(R) (2012).

[37] G. Rozas, A. E. Bruchhausen, A. Fainstein, B. Jusserand, and A. Lemaître, *Polariton Path to Fully Resonant Dispersive Coupling in Optomechanical Resonators*, Phys. Rev. B **90**, 201302(R) (2014).

[38] M. M. de Lima, M. van der Poel, P. V. Santos, and J. M. Hvam, *Phonon-Induced Polariton Superlattices*, Phys. Rev. Lett. **97**, 045501 (2006).

[39] E. A. Cerda-Méndez, D. N. Krizhanovskii, M. Wouters, R. Bradley, K. Biermann, K. Guda, R. Hey, P. V. Santos, D. Sarkar, and M. S. Skolnick, *Polariton Condensation in Dynamic Acoustic Lattices*, Phys. Rev. Lett. **105**, 116402 (2010).

[40] A. V. Scherbakov, T. Berstermann, A. V. Akimov, D. R. Yakovlev, G. Beaudoin, D. Bajoni, I. Sagnes, J. Bloch, and M. Bayer, *Ultrafast Control of Light Emission from a Quantum-Well Semiconductor Microcavity Using Picosecond Strain Pulses*, Phys. Rev. B **78**, 241302(R) (2008).

[41] T. Berstermann, A. V. Scherbakov, A. V. Akimov, D. R. Yakovlev, N. A. Gippius, B. A. Glavin, I. Sagnes, J. Bloch, and M. Bayer, *Terahertz Polariton Sidebands Generated by Ultrafast Strain Pulses in an Optical Semiconductor Microcavity*, Phys. Rev. B **80**, 075301 (2009).

[42] T. Berstermann, C. Brüggemann, A. V. Akimov, M. Bombeck, D. R. Yakovlev, N. A. Gippius, A. V. Scherbakov, I. Sagnes, J. Bloch, and M. Bayer, *Destruction and Recurrence of Excitons by Acoustic Shock Waves on Picosecond Time Scales*, Phys. Rev. B **86**, 195306 (2012).

[43] D. H. O. Machado, A. Crespo-Poveda, A. S. Kuznetsov, K. Biermann, L. V. A. Scalvi, and P. V. Santos, *Generation and Propagation of Superhigh-Frequency Bulk Acoustic Waves in GaAs*, Phys. Rev. Applied **12**, 044013 (2019).

[44] O. Kyriienko, T. C. H. Liew, and I. A. Shelykh, *Optomechanics with Cavity Polaritons: Dissipative Coupling and Unconventional Bistability*, Phys. Rev. Lett. **112**, 076402 (2014).

[45] K. M. Lakin, *Thin Film Resonator Technology*, IEEE Trans. Ultrason. Ferroelectr. Freq. Control **52**, 707 (2005).

[46] P. Dular, C. Geuzaine, F. Henrotte, and W. Legros, *A General Environment for the Treatment of Discrete Problems and Its Application to the Finite Element Method*, IEEE Trans. Magn. **34**, 3395 (1998).

[47] F. Iikawa, A. Hernández-Mínguez, M. Ramsteiner, and P. V. Santos, *Optical Phonon Modulation in Semiconductors by Surface Acoustic Waves*, Phys. Rev. B **93**, 195212 (2016).

[48] T. Sogawa, P. V. Santos, S. K. Zhang, S. Eshlaghi, A. D. Wieck, and K. H. Ploog, *Dynamic Band-Structure Modulation of Quantum Wells by Surface Acoustic Waves*, Phys. Rev. B **63**, 121307(R) (2001).

[49] *Landolt-Börnstein*, edited by O. Madelung (Springer Verlag, London, 1982), Vol. 17a.

[50] F. Iikawa, A. Hernández-Mínguez, I. Aharonovich, S. Nakhaie, Y.-T. Liou, J. M. J. Lopes, and P. V. Santos, *Acoustically Modulated Optical Emission of Hexagonal Boron Nitride Layers*, Appl. Phys. Lett. **114**, 171104 (2019).

[51] E. A. Cerda-Méndez, D. N. Krizhanovskii, K. Biermann, R. Hey, M. S. Skolnick, and P. V. Santos, *Wavefunction of Polariton Condensates in a Tunable Acoustic Lattice*, New J. Phys. **14**, 075011 (2012).

[52] D. L. Chafatinos, A. S. Kuznetsov, S. Anguiano, A. E. Bruchhausen, A. A. Reynoso, K. Biermann, P. V. Santos, and A. Fainstein, *Polariton-Driven Phonon Laser*, Nat. Commun. **11**, 4552 (2020).

[53] M. Hamoumi, P. E. Allain, W. Hease, E. Gil-Santos, L. Morgenroth, B. Gérard, A. Lemaître, G. Leo, and I. Favero, *Microscopic Nanomechanical Dissipation in Gallium Arsenide Resonators*, Phys. Rev. Lett. **120**, 223601 (2018).

[54] C. Schneider, K. Winkler, M. D. Fraser, M. Kamp, Y. Yamamoto, E. A. Ostrovskaya, and S. Höfling, *Exciton-Polariton Trapping and Potential Landscape Engineering*, Rep. Prog. Phys. **80**, 016503 (2017).

[55] A. S. Kuznetsov, P. L. J. Helgers, K. Biermann, and P. V. Santos, *Quantum Confinement of Exciton-Polaritons in Structured (Al,Ga)As Microcavity*, Phys. Rev. B **97**, 195309 (2018).

[56] S. Anguiano, A. E. Bruchhausen, B. Jusserand, I. Favero, F. R. Lamberti, L. Lanco, I. Sagnes, A. Lemaître, N. D. Lanzillotti-Kimura, P. Senellart, and A. Fainstein, *Micropillar Resonators for Optomechanics in the Extremely High 19–95-GHz Frequency Range*, Phys. Rev. Lett. **118**, 263901 (2017).

[57] D. Bajoni, P. Senellart, E. Wertz, I. Sagnes, A. Miard, A. Lemaître, and J. Bloch, *Polariton Laser Using Single Micropillar GaAs-GaAlAs Semiconductor Cavities*, Phys. Rev. Lett. **100**, 047401 (2008).

[58] R. I. Kaitouni, O. El Daïf, A. Baas, M. Richard, T. Paraiso, P. Lugan, T. Guillet, F. Morier-Genoud, J. D. Ganière, J. L. Staehli, V. Savona, and B. Deveaud, *Engineering the Spatial Confinement of Exciton Polaritons in Semiconductors*, Phys. Rev. B **74**, 155311 (2006).

[59] A. Bojahr, M. Gohlke, W. Leitenberger, J. Pudell, M. Reinhardt, A. von Reppert, M. Roessle, M. Sander, P. Gaal, and M. Bargheer, *Second Harmonic Generation of Nanoscale Phonon Wave Packets*, Phys. Rev. Lett. **115**, 195502 (2015).

[60] A. Amo and J. Bloch, *Exciton-Polaritons in Lattices: A Non-Linear Photonic Simulator*, C.R. Phys. **17**, 934 (2016).

[61] Y. Pennec, J. O. Vasseur, B. Djafari-Rouhani, L. Dobrzyński, and P. A. Deymier, *Two-Dimensional Phononic Crystals: Examples and Applications*, Surf. Sci. Rep. **65**, 229 (2010).